

AMB2025-03 High-Cycle Rotating Bending Fatigue Tests of PBF-L Ti-6Al-4V

Nik Hrabe¹, Jake Benzing¹, Newell Moser¹, Nick Derimow¹, Orion Kafka¹, Alec Saville¹, Ed Glaessgen², John Andrew Newman², Sai Yeratapally², Josh Pribe², George Weber², Sang-Hyon Chu², Rick Rogers³, Cassidy Allen⁴, Edwin Glaubitz⁵

¹*National Institute of Standards and Technology (NIST), Boulder, CO, USA*

²*NASA Langley Research Center, Hampton, VA, USA*

³*NASA Glenn Research Center, Cleveland, OH, USA*

⁴*University of Colorado-Boulder, Boulder, CO, USA*

⁵*Colorado School of Mines, Golden, CO, USA*

CHALLENGE SUMMARY

Specimens from one build of laser powder bed fusion (PBF-L) titanium alloy (Ti-6Al-4V) were split equally into two heat treatment conditions. The first condition is a non-standard hot isostatic pressing (HIP) heat treatment (800 °C, 2 h, argon pressure of 200 MPa, approximately 12 °C/min cooling rate), which will be referred to as 800HIP. The second condition is the same heat treatment but in a vacuum furnace with a partial pressure of argon (75 mTorr) and will be referred to as 800VAC. All fatigue specimens were vertically oriented during PBF-L, then after post-processing was completed, the specimens were machined and polished to remove the as-built surface roughness and PBF-LB contour. Approximately 25 specimens per condition were tested in high-cycle fully reversed 4-point rotating bending fatigue (RBF, R = -1) according to ISO 1143.

Calibration data given for both conditions will include: detailed build parameters, heat treatment details (time, temperature, and chamber pressure), solid chemistry, surface roughness measurements of the gauge section of fatigue specimens, strain measured in gauge section of fatigue specimens via x-ray diffraction (XRD), 2D maps of grain size and morphology via scanning electron microscopy (SEM), 2D crystallographic texture via electron backscatter diffraction (EBSD), pore size and spatial distribution via x-ray computed tomography (XCT), and quasi-static tensile properties according to ASTM E8. All fatigue data (S-N curve) for the 800HIP condition will also be given as calibration data. See detailed description of the calibration data below.

Predictions for the 800VAC condition include (1) S-N curve, (2) specimen-specific fatigue strength, and (3) specimen-specific fatigue crack initiation locations. Predictions must utilize the prediction submission template found in this dataset (<https://doi.org/10.18434/mds2-3734>), must be submitted via email to AMBench@nist.gov (subject: AMB2025-03 prediction submission), and must be submitted by 11:59pm ET, August 29, 2025. Email nik.hrabe@nist.gov if you have problems accessing this dataset.

MATERIALS AND METHODS

Build and Powder Details

Ti-6Al-4V material was built on a 3D Systems DMP Flex 350 machine¹ (software version 36.15.13). Standard build parameters were used: 60 μm layer height, beam spot size 80 μm , no baseplate preheating, 99.999% argon build atmosphere, 245 W laser power, 1250 mm/s scan speed, 245 degree scan rotation between layers. Standard plasma atomized spherical powder was used: 10-45 μm powder size range, D10 21 μm , D50 35 μm , D90 47 μm . More build and powder details can be found in the dataset. Vertically oriented cylinders (approximately 15 mm diameter x 105 mm length) were numbered according to the build layout shown in Figure 1. All specimen numbers in this dataset refer to these build layout identification numbers.

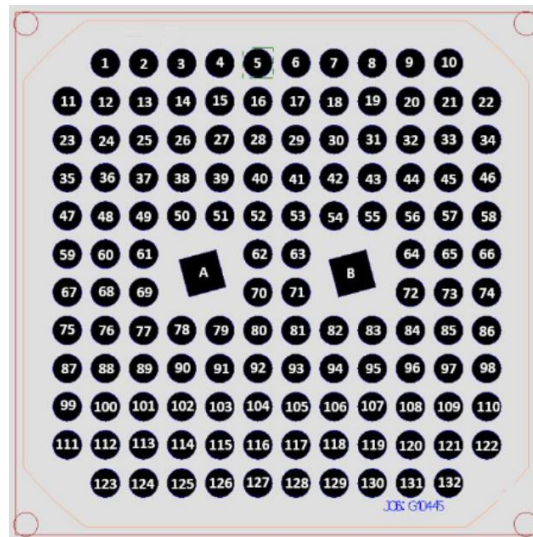


Figure 1: Top view of build showing specimen identification numbers. Bottom of image corresponds to front of machine. Raking direction is horizontal in image (bi-directional raking). Gas flow is from bottom to top in image (front to back in machine).

Heat Treatment

The post-processing treatments were designed to maintain similar grain structure characteristics and the major difference in the microstructure is the sealing of internal porosity in the HIP condition via isostatic pressure. A high-pressure low temperature hot isostatic pressing treatment that has gained attention in the past few years was employed in this work. The post-processing in a HIP vessel used a heating rate of 12 $^{\circ}\text{C}/\text{min}$ cooling rate, hold temperature of 800 $^{\circ}\text{C}$, hold time of 2 h with an argon pressure of 200 MPa, and a cooling rate of 12 $^{\circ}\text{C}/\text{min}$. This condition is deemed 800HIP. The second condition uses the same hold temperature, hold time, and desired cooling rate, but was conducted in a vacuum furnace with a partial pressure of argon (approximately 75 mTorr). In Figure 2, the time-temperature-pressure data is presented. The cooling rates were measured between 775 $^{\circ}\text{C}$ and 550 $^{\circ}\text{C}$, yielding a cooling rate of 10.3 $^{\circ}\text{C}/\text{min}$ in the 800VAC condition and 11.7 $^{\circ}\text{C}/\text{min}$ cooling rate in the 800HIP condition.

¹ Certain commercial equipment, instruments, or materials are identified in this paper in order to specify the experimental procedure adequately. Such identification is not intended to imply recommendation or endorsement by NIST, nor is it intended to imply that the materials or equipment identified are necessarily the best available for the purpose.

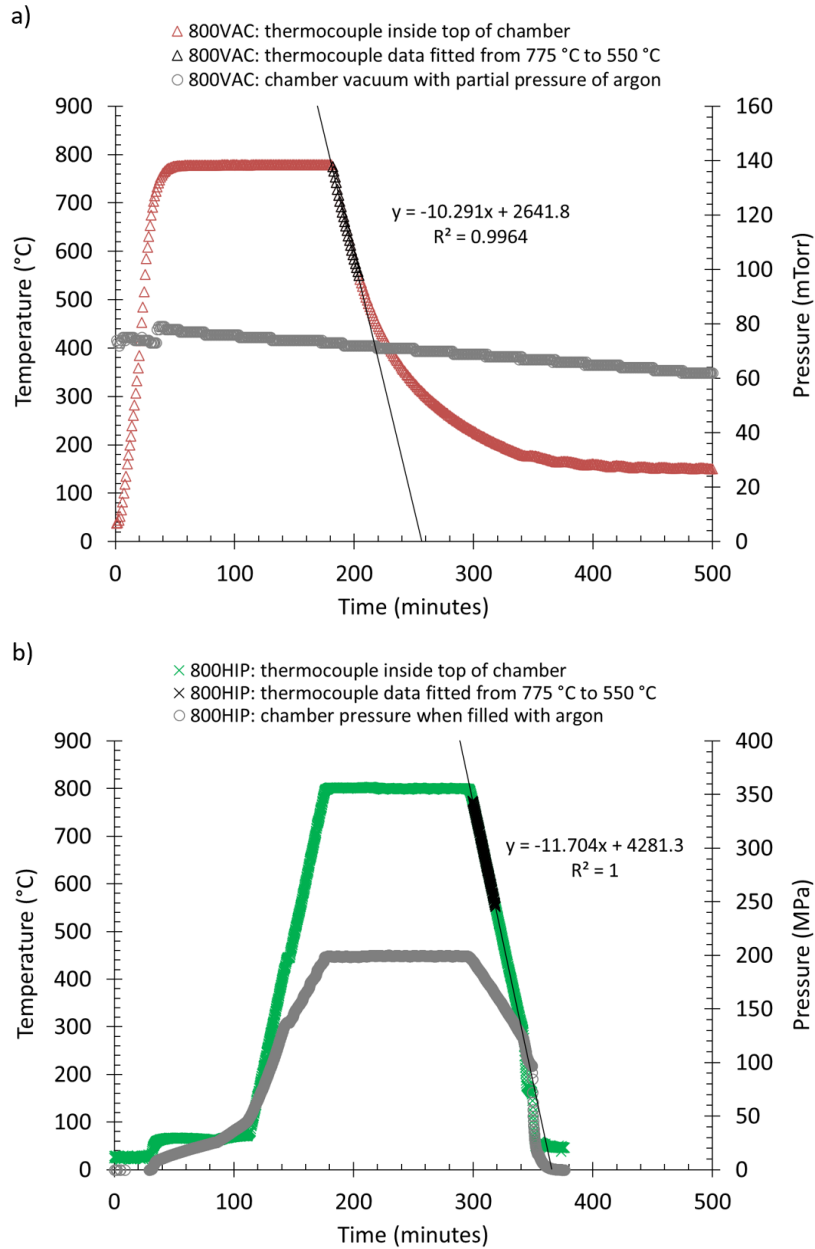


Figure 2: Post-processing conditions for the a) 800 VAC condition where temperature and environment pressure are plotted versus time and the b) 800HIP condition where temperature and isostatic pressure of argon are shown versus time.

Solid Chemistry

Chemistry was measured for solid material after heat treatment and surface removal, and results are shown in Table 1. There is no appreciable difference in chemistry between the two conditions, and both conditions meet material specification ASTM F3001.

Table 1: Solid chemistry measurements (wt%) of both conditions compared to material specification ASTM F3001.

condition	Al (wt%)	V (wt%)	O (wt%)	C (wt%)	N (wt%)	H (wt%)	Fe (wt%)
ASTM F3001	5.50-6.50	3.50-4.50	0.13 max	0.08 max	0.05 max	0.012 max	0.25 max
800HIP-106	6.30	3.89	0.10	0.01	0.02	0.003	0.16
800VAC-85	6.30	3.76	0.10	0.01	0.02	0.003	0.17

Specimen Preparation

After heat treatment, cylinders were machined and polished according to ISO 1143. The final specimen geometry is shown in Figure 3, and these specimens were used for both tensile and fatigue testing.

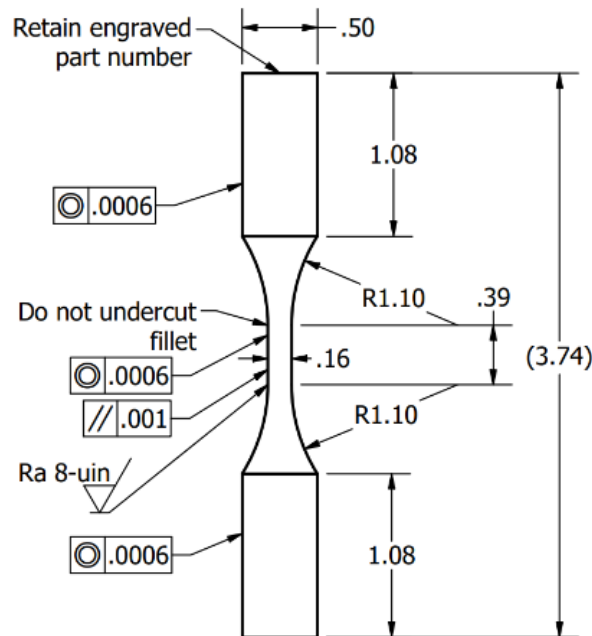


Figure 3: Schematic showing specimen geometry and dimensions (all in inches). This specimen was used for both tensile and fatigue testing.

Profilometry

Surface roughness was measured on the gauge section of multiple specimens from both conditions, and it was confirmed (Table 2) all specimens meet ISO 1143 surface roughness requirement (maximum 0.2 μm Ra). More surface roughness parameter measurements can be found in the full dataset. Gauge section roughness was measured using an Olympus OLS-5100 laser scanning confocal microscope with a 50x objective with 0.95 numerical aperture and 0.256 μm pixel spacing and 0.12 μm z-pitch (spacing between height images). A 3d stitched image using 1x22 fields of view with 10% overlap (5110 μm long and 256 μm wide stitched image size) between images was acquired. From the stitched image, 5 line profiles were selected to be approximately equally spaced along the width of the measurement. The line profiles were filtered using tilt removal, 2500 μm form removal (λ_f), long wavelength cutoff (λ_c) of 800 μm , and short wavelength cutoff (λ_s) of 2 μm .

Table 2: Surface roughness results from measurements of the gauge section of multiple specimens from both conditions. All specimens meet ISO 1143 surface roughness requirements (maximum 0.2 $\mu\text{m Ra}$).

Specimen	avg. Ra (μm)	std. dev. (μm)
HIP-42	0.094	0.005
HIP-58	0.120	0.008
HIP-66	0.133	0.016
VAC-1	0.104	0.011
VAC-97	0.089	0.008

Scanning Electron Microscopy

Samples were metallographically prepared by cross-sectioning RBF runout gauge sections in the XY and Z directions, shown schematically and pictorially in Figure 4.

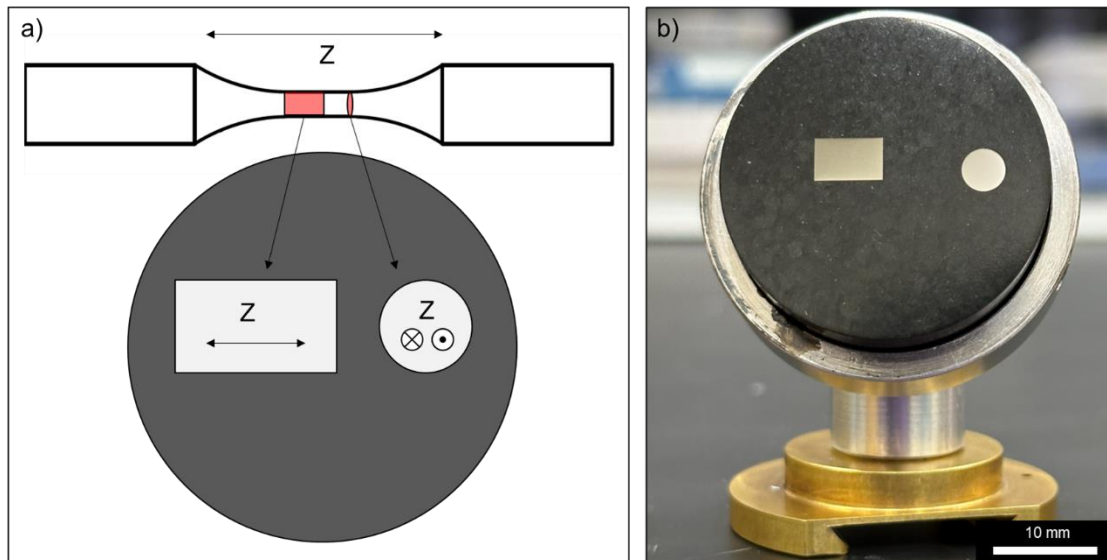


Figure 4: Schematic showing metallographic mounting orientation relative to the rotating bending fatigue specimens. a) Schematic of the mounting directions relative to the build direction (Z) *note, the red circle is perpendicular to Z. b) Picture of the mounted specimens in an SEM-EBSD pre-tilted specimen holder.

Scanning electron microscopy (SEM) was carried out via backscatter electron (BSE) imaging on a field emission SEM for the HIP and VAC conditions at an accelerating voltage of 20 kV. Three different magnification images were collected for both conditions in the XY and Z planes. Fractography was conducted on all RBF specimens via optical microscopy. Fractography via secondary electron (SE) SEM was carried out at an accelerating voltage of 20 kV on the VAC samples brought to failure to cross-reference the pore-initiating failure locations via XCT. SEM-based fractography was also carried out on a HIP specimen to confirm surface-based crack initiation.

In addition, electron backscatter diffraction measurements were performed on both VAC and HIP samples across the XY and Z planes (Figure 4b). Before measurements, plasma cleaning was conducted for 15 minutes. Then a field emission SEM operated with a 25 kV accelerating voltage, with a 120 μm aperture, a 19 mm working distance, a magnification of 300 X, and a dynamic focus of 2.5% was used to setup the SEM environment. During EBSD acquisition with TSL OIM Data Collection 7 software, camera exposures were optimized for confidently indexing of diffraction patterns the typical frame rate used was 130 frames per second with minimal gain required (8 out of 700). Only the α -Ti hexagonal

phase was indexed during a multi-tile mapping acquisition. Each tile was roughly 290 μm x 290 μm , indexed with a 0.35 μm step size, and 16 tiles (4x4) were mapped with a 5% overlap, resulting roughly 10 million diffraction patterns indexed. Data sets were analyzed using TSL OIM Analysis versions 8 and 9, by stitching the 16 tiles together, cropping of edges of the completed map, then routine cleaning procedures were performed: grain confidence index (CI) standardization, neighbor CI correlation, neighbor orientation correlation, and grain dilation.

X-ray Computed Tomography

A Zeiss Xradia Versa XRM-500 was used to perform X-ray computed tomography (XCT). The entire gauge sections of five rotating beam fatigue (RBF) specimens were measured using XCT. Note, the XCT measurements were taken prior to the fatigue experiments. To image the RBF specimens, four fields-of-view (FOV) were taken along the gauge section with at least 20% overlap. The reconstructed images of these four FOVs were then vertically stitched together into a single, larger stack of images. While the resultant image stack differs between the RBF specimens, the number of images in each of the final image stacks is typically greater than 3200 images, and each individual image is typically 1004 pixels wide by 1024 pixels tall. The pixel size, or resolution, of the XCT measurements was $5.50 \pm 0.16 \mu\text{m}/\text{pixel}$.

The key parameters of the XCT measurements are given in Table 3. The radiographs taken for each FOV were reconstructed using the Zeiss proprietary software, Reconstructor Scout-and-Scan (version 14.0.1), with drift corrections accounted for via adaptive motion compensation. We assume that the reconstruction algorithm is based on the popular Feldkamp-Davis-Kress (FDK) cone-beam reconstruction algorithm [Feldkamp].

Table 3: Summary of the nominal XCT parameters.

Accelerating voltage	140 kV
Accelerating amperage	71 μA
Radiograph exposure time	4.0 s
Voxel edge length	5.50 μm
Radiographs taken about 360°	1601
Image bit depth	16-bit
Zeiss filter	HE2
Beam hardening correction factor	0.25

A fiducial was required in order to register the XCT data with the optical images taken during the fractographic examination. For this purpose, a small droplet of pink, polymer-based lacquer (i.e., nail polish) was applied to the surface of the RBF specimen along the gauge section. The droplet of lacquer contained lead particles, approximately 300 μm in diameter, in a volume ratio of less than 20% lead powder. The dense particles in the lacquer were easily spotted in the XCT measurements, and similarly, the pink color of the lacquer was easily spotted in the optical microscopy images. The fiducial droplet was approximately 1 mm in diameter, and none of the RBF specimens fractured at the fiducial. After the RBF specimen broke, the relative length and angular position was approximately measured between the fiducial and the killer defect. This positional information, in combination with the shape of the killer defect, were then used to identify the labeled pore from the XCT dataset.

After the XCT radiographs were reconstructed, additional image post-processing was performed, including segmentation of the pores. Image post-processing and segmentation was accomplished using

Python scripts and the open-source library, IMPPY3D [Moser]. The reconstructed data for each of RBF specimens was post-processed in the same way. An overview of the post-processing steps is described next. However, the reader is referred to the calibration data for additional details about the post-processing and the associated Python scripts.

The reconstructed, 16-bit radiographs were denoised using a non-local means denoising algorithm and then converted to 8-bit grayscale images. Due to the cone-beam effect of the X-ray source, the grayscale intensities were inconsistent for some images near the ends of the image stack. So, the first and last 60 images were removed for the remainder of the post-processing of the image stacks. Next, the images were segmented (i.e., binarized) using hysteresis thresholding, resulting in white pixels corresponding to metallic material and black pixels corresponding to air.

After segmentation, additional post-processing was performed to fully enclose near-surface features, otherwise they would not be identified and labeled in future steps. This proved to be an important step since near-surface features frequently play a critical role in RBF experiments. First, for each 2D image, the lead particles associated with the fiducial were removed using an inverted, circular mask. The size of circular mask closely matched the diameter of the circular cross-sections of the RBF specimen. Next, the convex hull was calculated and drawn (in white pixels) for each 2D image. Drawing the perimeter of the convex hull ensures that concave surface features are fully enclosed and will be labeled in subsequent steps. While this modified image stack will be used for labeling features and pores, two binarized image stacks will be provided for each RBF specimen: the first image stack is an unmodified segmentation, and the second image stack is the modified segmentation that includes the drawn convex hull.

Using the segmented images with the convex hull drawn, fully enclosed pores were identified and numerically labeled. Individual pores were identified using 1-connectivity. Then, additional metrics for each pore, such as its centroid and equivalent spherical diameter, were calculated and saved into a CSV file. The segmented images were also converted into VTK files, thereby enabling 3D visualization using ParaView [Ayachit].

X-ray Diffraction

X-ray diffraction (XRD) was carried out using a Cu K α source at a step size of 0.01° from 30° to 80° 2 θ . Macroscopic XRD was carried out on the gauge Figure 5a using Bragg-Brentano geometry and approximate spot size of 5 mm x 5 mm. The microscopic XRD Figure 5b was collected on the gauge section using parallel beam geometry and micro area slits resulting in a spot size of approximately 2 mm x 1 mm. This same optical setup was utilized for internal measurements of the gauge section Figure 5c of the metallographically mounted cross section.

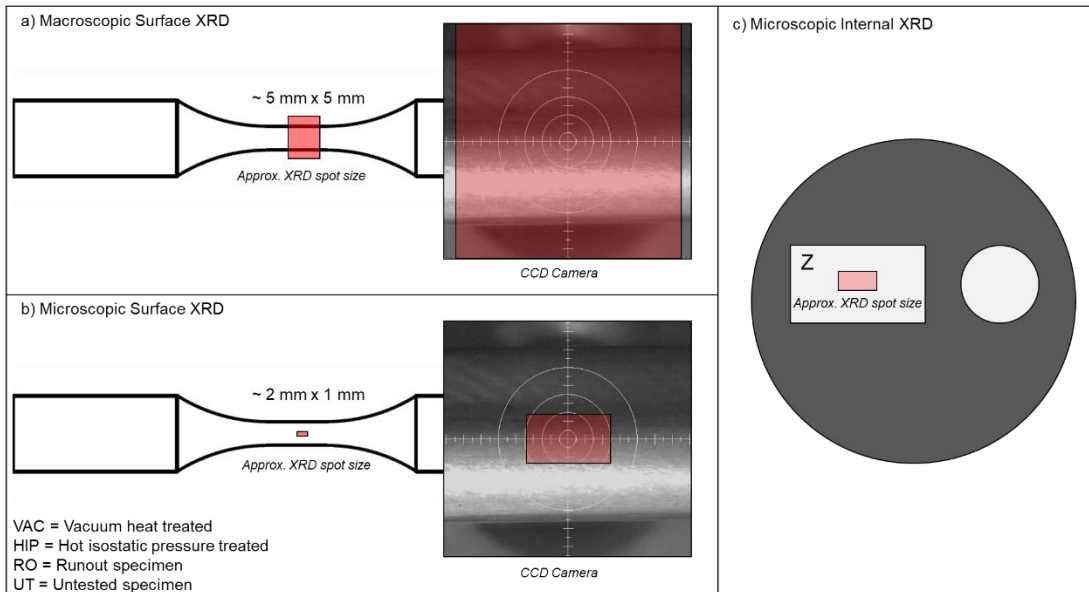


Figure 5: Schematic showing metallographic mounting orientation relative to the rotating bending fatigue specimens. a) Schematic of the mounting directions relative to the build direction (Z) *note, the red circle is perpendicular to Z. b) Picture of the mounted specimens in an SEM-EBSD pre-tilted specimen holder.

Tensile Testing

Three specimens from each condition were tensile tested according to ASTM E8 on a servo-hydraulic load frame under displacement control at quasi-static strain rate (0.001 /s) and using a contact extensometer (gauge length 6 mm). The linear variable differential transformer (LVDT) and load cell (25kN capacity) were calibrated less than a year before the test date resulting in sufficiently small error. The calibration of the extensometer was completed before testing, which was performed using an Epsilon Model 3590VHR Displacement Calibrator. The verification resulted in a maximum error of less than 1% through a range of 0% to 100% of total extension. The diameter of each specimen was measured prior to testing using calipers, which have a rated accuracy of $\pm 0.01\text{mm}$. The Young's modulus was calculated from the slope of the linear region in the stress-strain data via an analysis of residuals in accordance with ASTM E3076.

Fatigue Testing

Twenty-four specimens from each condition were tested in four-point rotating bending fatigue (RBF) using an ADMET eXpert 9313 (test frequency 100 Hz, load ratio $R = -1$) fatigue testing machine according to ISO 1143. The load cell (50 lbf capacity) and rotational speed were calibrated less than a year before the final test date resulting in sufficiently small error. The diameter of each specimen was measured prior to testing using calipers, which have a rated accuracy of $\pm 0.01\text{mm}$.

CALIBRATION DATA

Scanning Electron Microscopy

SEM-BSE images are shown in Figure 6 of the VAC and HIP conditions. The images were taken parallel to the XY plane (Figure 6a and Figure 6c) and Z plane (Figure 6b and Figure 6d). The darker laths are of the HCP α phase, whereas the lighter regions constrained within these laths are BCC β phase. The contrast between the two phases is dictated by the elemental chemistry, such that phases with an overall higher Z (e.g., V-rich β phase) will appear brighter than the Al-rich α phase. There are no clear differences between the microstructure of the VAC and HIP conditions as observed via SEM-BSE.

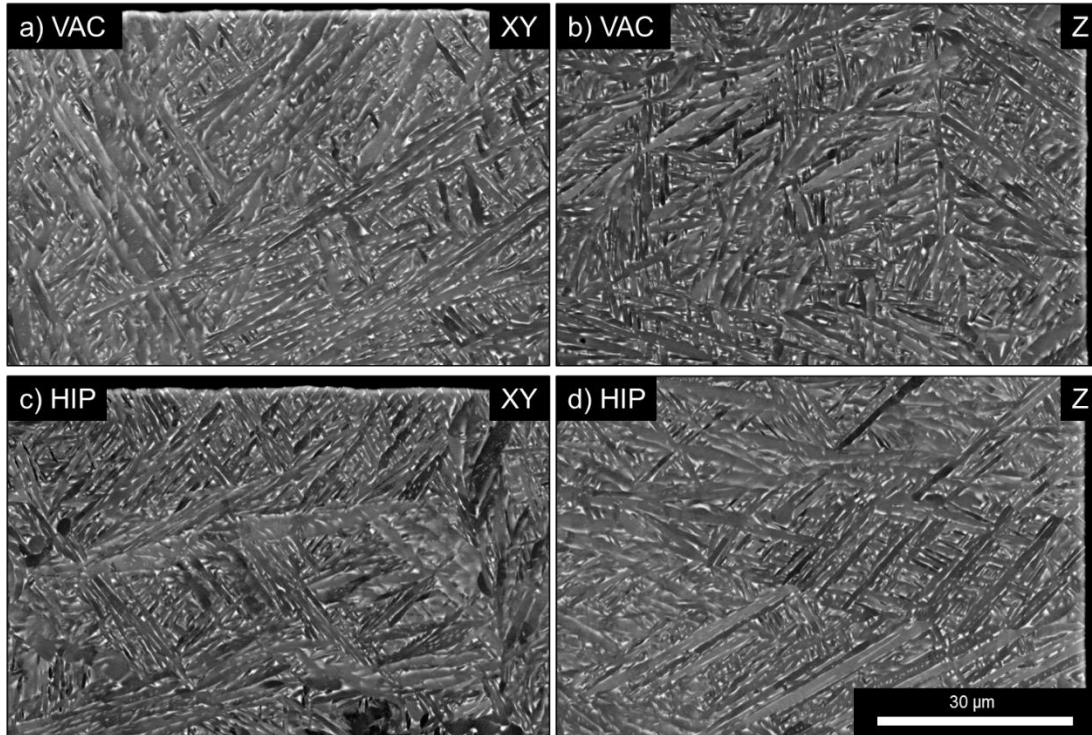


Figure 6: SEM-BSE images taken parallel to the XY (Z in/out of screen) and Z (up/down the screen) planes for both HIP and VAC conditions. a) XY plane of VAC, b) Z plane of VAC, c) XY plane of HIP, d) Z plane of HIP. The black regions are the sample edges.

The SEM-based measurements acquired via EBSD were performed on XY and XZ planes for both 800VAC and 800HIP conditions. One purpose of using similar post-processing parameters (temperature, hold time, and cooling rate) was to produce equivalent grain structures and leave porosity (800VAC) as a control variable (removed in 800HIP). All EBSD raw data, stitched and cleaned multi-tile data sets, maps, and histograms are provided as calibration data for all planes and conditions. The list of maps and histograms includes: kernel average misorientation, grain reference orientation deviation, inverse pole figure, image quality, unique grain identity, grain size area, and all appropriate legends/scales. One example, the inverse pole figure map, is shown for one plane from both conditions in Figure 7a/b, where the Z direction (build direction) is parallel to the horizontal direction of the image. Influences of the layer-by-layer PBF-L process on grain orientation and morphology is still evident after post-processing due to hold temperature (below the β transus for Ti-6Al-4V). Also, an over simplified grain size metric (area of an α lath) is presented in Figure 7c and shows a near identical distribution of grain area for both conditions with the average grain areas being $25.06 \mu\text{m}^2$ and $24.13 \mu\text{m}^2$, respectively in the 800VAC and 800HIP conditions.

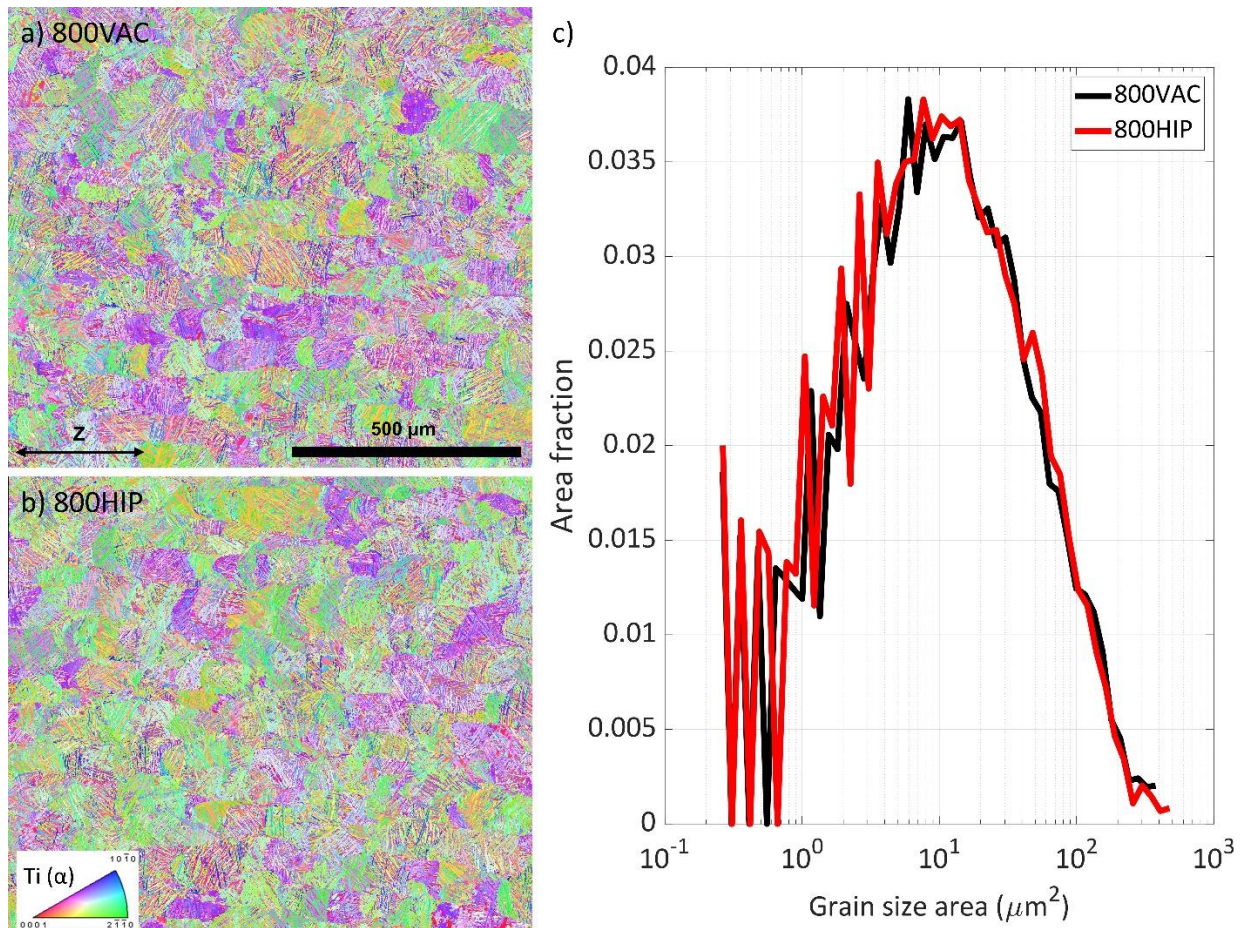


Figure 7: EBSD measurements exported to produce an a) inverse pole figure map from the XZ plane on the 800VAC sample and an b) inverse pole figure map from the XZ plane on the 800HIP sample, where Z is the build direction, only a titanium phase was indexed and the stitched multi-tile maps cover the same area. A comparison of a single grain size metric is shown in where c) grain size area of each α titanium lath is binned and the distribution is shown on a log-scale (x-axis only) for both conditions.

X-ray Computed Tomography

X-ray computed tomography (XCT) data along various levels of post-processing have been completed to assist with predicting the location of failure and predicting the cycles to failure of the RBF specimens. However, participants are of course free to perform their own image post-processing techniques. The following X-ray computed tomography (XCT) data are provided for each RBF specimen:

1. The binary, Zeiss project files which include the X-ray radiographs of each field-of-view. These files are saved as Zeiss .xrm and .txrm file formats which will require either Zeiss software or additional libraries/software to parse successfully.
2. The unaltered, reconstructed image stack after vertical stitching (as grayscale 16-bit images). Recall that the entire gauge section of an RBF specimen required four fields-of-view.
3. Denoised version of the reconstructed image stack (as grayscale 8-bit images).
4. Two segmented image stacks of the RBF specimens; solid (or metallic) materials are represented by white pixels and the remaining pixels are black. One image stack is unaltered after applying

the thresholding criterion. The other image stack was modified to include the perimeter of the convex hull, which fully encloses surface features.

5. Two segmented image stacks of the pores; fully enclosed pores are represented by white pixels and the remaining pixels are black. One image stack is derived from the unaltered segmentation of the RBF specimen. The other image stack is derived from the modified segmentation that incorporated the convex hull.
6. Verification image stacks where the identified pores are superimposed as translucent red pixels on the denoised, grayscale images.
7. Labeled image stack that contains the identified pores as grayscale values. More specifically, the image stack is saved as unsigned 16-bit images, and each pore that has been given a numerical identifier is saved in this image stack with a grayscale intensity equal to its identifier. For example, the pore labeled "42" can be found by seeking pixels equal to an intensity of 42.
8. Two VTK files that can be opened and visualized using a program like ParaView. The first is a mesh representing the boundaries of the RBF specimen. The second is a voxel model that includes all of the identified pores and features. Field variables have been included in this voxel model which provide information about the individual pores, such as equivalent spherical diameter, volume, centroid coordinates, etc.
9. A comma-separated value (CSV) containing the calculated porosity of the region measured by XCT.
10. A CSV file containing the calculated cross-sectional area for each 2D image in the stack (i.e., as a function of gauge length).
11. A CSV file containing a list of the identified pores and any associated metrics that were calculated for said pore. For a full description of these quantities, see the ReadMe file in the calibration data. A few of the key metrics of each pore that can be found in this file include: the feature label (or identifier), the centroid coordinates, the volume of the pore, the equivalent spherical diameter, the sphericity, and the extent of the pore given as quantities associated with its rotated bounding box.

For these challenges, we ask that participants use the provided Excel template submission forms. Regarding the prediction of the failure location for a given RBF specimen, participants will be asked to provide the feature ID numbers associated with the pores they believe to be most likely the killer defect. More specifically, participants will be able to provide four feature IDs (i.e., four guesses), and if any of these guesses correctly identify the real killer defect, then full points will be awarded. The feature IDs of the pores can be found in the provided CSV files containing the calculated pore metrics, in the VTK voxel models, and in the labeled image stacks – see the above list of provided data for more information about these files.

When choosing a feature ID for submission, we wish to remind participants to double-check that the chosen feature is "real". We have tried our best to ensure the accuracy of these segmentations, but there are thousands of images to verify. We cannot guarantee that every labeled feature corresponds to real pores or surface defects in the physical part. For example, the lead particles used in the fiducial mark unexpectedly created X-ray shadows in the reconstructed images which have occasionally been

identified by the segmentation scripts as surface defects. We have carefully chosen the segmentation parameters so as to minimize these artifacts, but some may still exist. Before submitting your finalized guesses, we recommend visually checking the original grayscale images to verify that the feature in question is not actually a result of XCT artifacts. Furthermore, none of the RBF specimens fractured through the fiducial mark.

X-ray Diffraction

The raw XRD of the macroscopic data taken from runout (RO) specimens is shown in Figure 8a and cleaned using a Savitzky-Golay filter in Figure 8b. A zoomed in view of the cleaned data is shown between 32° to 42° 2θ in Figure 8c, plus Figure 8d is of microscopic measurements/ cleaned data of untested (UT) specimen gauge sections and internal microscopic measurements of the mounted metallographic cross sections.

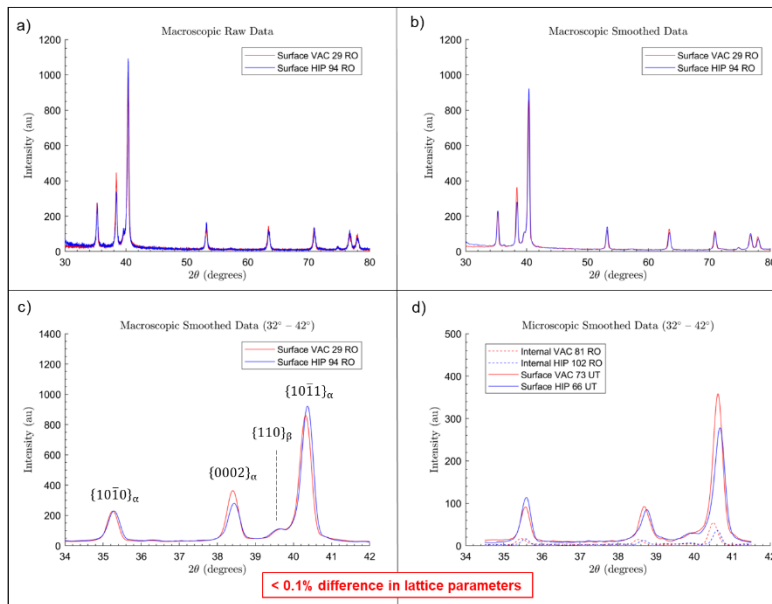


Figure 8: a) Raw XRD data of the macroscopic measurements of the runout gauge sections for both VAC and HIP. b) Cleaned data using a Savitzky-Golay filter. c) Zoomed in range between 32° to 42° 2θ of the cleaned data. d) Cleaned micro area microscopic measurements of both internal (XY plane) and surface (gauge section in the Z direction).

Tensile

Tensile results for both conditions are shown in Table 4. There are no statistically significant differences ($p < 0.05$) between the two conditions for any of the properties measured.

Table 4: Tensile results, including statistics for both conditions. There are no statistically significant differences ($p < 0.05$) between the conditions for yield strength (YS), ultimate tensile strength (UTS), elastic modulus, uniform elongation, or total elongation.

Specimen	Diameter (mm)	YS (MPa)	UTS (MPa)	Elastic Modulus (GPa)	Uniform Elongation (%)	Total Elongation (%)
HIP-02	4.10	1018.5	1091.0	152	5.2	22.8
HIP-50	4.10	998.4	1094.2	150	6.1	20.2
HIP-74	4.11	997.5	1083.3	157	4.2	15.3
average	4.10	1004.8	1089.5	153	5.2	19.4
stdev	0.01	11.9	5.6	3	1.0	3.8

Specimen	Diameter (mm)	YS (MPa)	UTS (MPa)	Elastic Modulus (GPa)	Uniform Elongation (%)	Total Elongation (%)
VAC-41	4.07	1012.7	1078.5	151	6.7	17.8
VAC-49	4.09	1007.3	1078.7	150	7.9	17.6
VAC-101	4.11	978.7	1090.6	149	3.9	11.5
average	4.09	999.6	1082.6	150	6.2	15.6
stdev	0.02	18.3	6.9	1	2.1	3.6

STATISTICS	unpaired t-test, two-tailed P-value	0.7011	0.2499	0.1757	0.4978	0.277
-------------------	--	---------------	---------------	---------------	---------------	--------------

Fatigue of 800HIP

Fatigue results for the 800HIP condition are shown in Figure 9. Results for 800VAC condition are not shown as they are the focus of requested predictions.

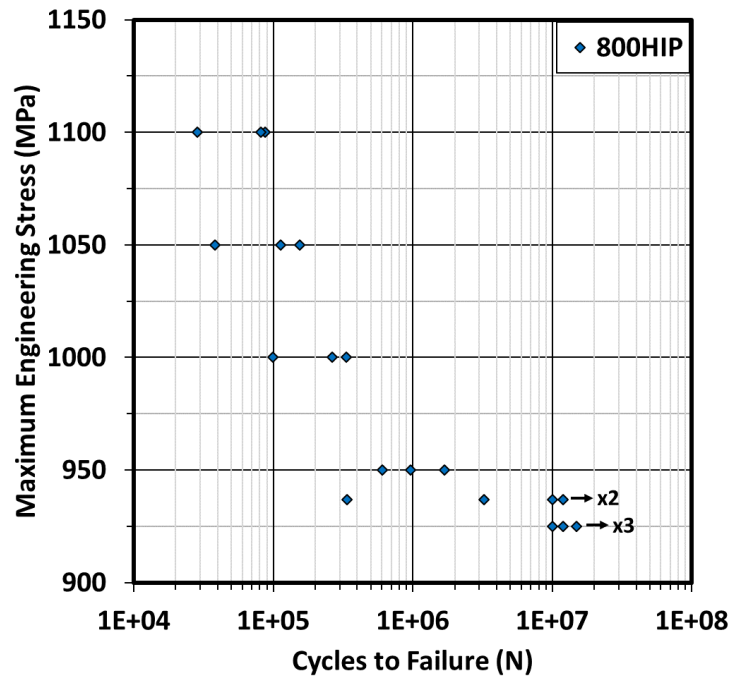


Figure 9: Fatigue S-N curve for 800HIP condition. Results for 800VAC condition are not shown as they are the focus of requested predictions.

Fractography

No HIP specimens were found to experience fatigue crack initiation at pores, as seen in Figure 10.

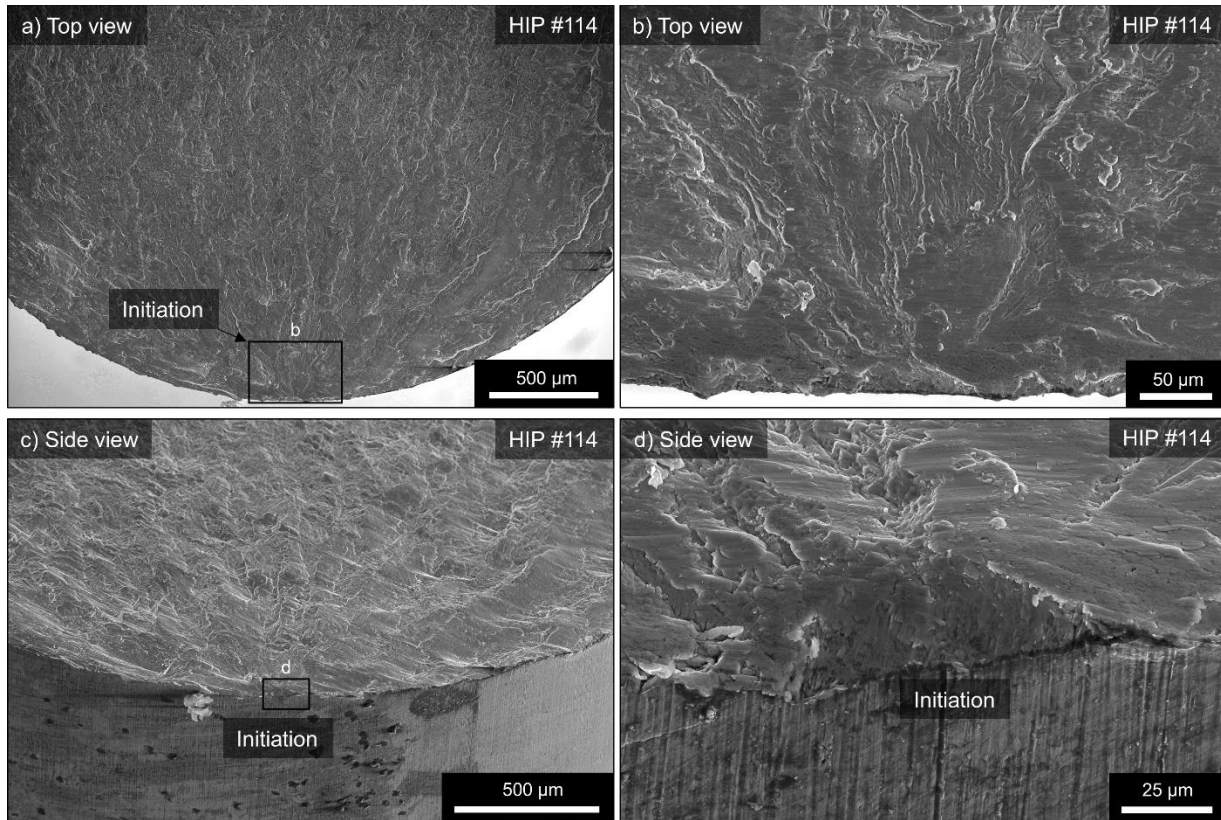


Figure 10: Fractography figure

PREDICTIONS REQUESTED and GRADING

See prediction template in dataset for specifics of each prediction, including grading. Predictions for the 800VAC condition include (1) S-N curve, (2) specimen-specific fatigue strength, and (3) specimen-specific fatigue crack initiation locations. Predictions must utilize the prediction submission template found in this dataset, must be submitted via email to AMBench@nist.gov (subject: AMB2025-03 prediction submission), and must be submitted by 11:59pm ET, August 29, 2025.

REFERENCES

U. Ayachit. (2015). "The ParaView Guide: A Parallel Visualization Application", Kitware, ISBN 9781930934306, <https://www.paraview.org/>

L.A. Feldkamp, L.C. Davis, and J.W. Kress. (1984). "Practical cone-beam algorithm," J. Opt. Soc. Am. A, 1, 612-619. <https://doi.org/10.1364/JOSAA.1.000612>

N.H. Moser, O.L. Kafka, A.K. Landauer. (2023). "IMPPY3D: 3D X-ray Computed Tomography Image Processing in Python," <https://github.com/usnistgov/imppy3d>, DOI:10.18434/mds2-2806